Complex pupil retrieval with undersampled data

Samuel T. Thurman[1,2,*] and James R. Fienup[1]

[1]*The Institute of Optics, University of Rochester, Rochester, New York 14627, USA*
[2]*Currently with Lockheed Martin Coherent Technologies, 135 South Taylor Avenue, Louisville, Colorado 80027, USA*
**Corresponding author: sam.t.thurman@lmco.com*

Received June 9, 2009; accepted October 12, 2009;
posted October 12, 2009 (Doc. ID 112485); published November 20, 2009

The ability to retrieve the complex-valued, generalized pupil function of an imaging system from undersampled measurements of the defocused system point spread function (PSF) is examined through numerical simulations. The ability to do so degrades as the detector pixel pitch increases when using a fixed number of PSF measurements. Two strategies for obtaining better results with undersampled data are demonstrated using additional PSF measurements with (i) random shifts due to system pointing fluctuations and (ii) intermediate amounts of defocus. © 2009 Optical Society of America

OCIS codes: 070.0070, 100.5070, 110.0110, 110.4850, 110.7350.

1. INTRODUCTION

Complex pupil retrieval is the method of estimating the generalized pupil function $P(\xi,\eta)$ (both amplitude and phase) of an imaging system from diverse measurements of the system point spread function (PSF) $s(x,y,d)$ [1–5]. When defocus is used for the diversity, these two quantities are related by [6]

$$s(x,y,d)=\left|\int_{-\infty}^{\infty}\int_{-\infty}^{\infty}P(\xi,\eta)\exp\left[\frac{-i2\pi}{\lambda f}(\xi x+\eta y)\right]\times\exp\left[\frac{-i8\pi d}{D^2}(\xi^2+\eta^2)\right]\mathrm{d}\xi\mathrm{d}\eta\right|^2, \tag{1}$$

where (ξ,η) are pupil coordinates, (x,y) are transverse spatial coordinates, λ is the wavelength of light, f is the system focal length, D is the encircled pupil diameter, and d is the amount of peak-to-valley defocus across the pupil of the system in units of wavelengths. The in-focus image plane location corresponds to $d=0$. In complex pupil retrieval, $P(\xi,\eta)$ is estimated from measurements of $s(x,y,d_k)$ made in a number of defocus planes indexed by $k\in\{1,2,\ldots,K\}$. One approach for doing this is to use an iterative nonlinear optimization algorithm to find the $P(\xi,\eta)$ that minimizes/maximizes a data consistency metric, which quantifies the agreement between the computed PSFs and the corresponding measured PSF data.

Let $g_{m,n,k}$ represent the measured PSF data, which is related to $s(x,y,d_k)$ by

$$g_{m,n,k}=\zeta_{m,n,k}+\int_{-\infty}^{\infty}\int_{-\infty}^{\infty}s(x-x_k,y-y_k,d_k)\times h_{\mathrm{d}}(n\Delta x-x,m\Delta y-y)\mathrm{d}x\mathrm{d}y, \tag{2}$$

where $\zeta_{m,n,k}$ is noise, $h_{\mathrm{d}}(x,y)$ is the detector-pixel impulse response function, Δx is the detector pixel pitch, and $m\in\{-N/2,(2-N)/2,\ldots,(N-2)/2\}$ and $n\in\{-N/2,(2-N)/2,\ldots,(N-2)/2\}$ are detector-pixel indices for even N. In practice, misregistrations (x_k,y_k) can originate from line-of-sight pointing fluctuations or misalignment of the defocusing mechanism, assumed here to be constant during any one exposure. The 2D discrete Fourier transform (DFT) of $g_{m,n,k}$,

$$G_{p,q,k}=\frac{1}{N}\sum_{m=-N/2}^{(N-2)/2}\sum_{n=-N/2}^{(N-2)/2}g_{m,n,k}\exp\left[\frac{-i2\pi}{N}(mp+nq)\right], \tag{3}$$

can be written in terms of continuous Fourier transforms as [7]

$$G_{p,q,k}=Z_{p,q,k}+N\sum_{\alpha=-\infty}^{\infty}\sum_{\beta=-\infty}^{\infty}\int_{-\infty}^{\infty}\int_{-\infty}^{\infty}S(u,v,d_k)\times\exp\left[\frac{-i2\pi}{N}(\hat{x}_k u+\hat{y}_k v)\right]H_{\mathrm{d}}(u,v)\times\mathrm{sinc}\left(\frac{p\Delta u-\alpha N\Delta u-u}{\Delta u}\right)\times\mathrm{sinc}\left(\frac{q\Delta u-\beta N\Delta u-v}{\Delta u}\right)\mathrm{d}u\mathrm{d}v, \tag{4}$$

where $Z_{p,q,k}$ is the 2D DFT of $\zeta_{m,n,k}$, $S(u,v,d_k)$ is the OTF for the kth PSF, $H_{\mathrm{d}}(u,v)$ is the 2D continuous Fourier transform of $h_{\mathrm{d}}(x,y)$, $\mathrm{sinc}(x)=\sin(\pi x)/(\pi x)$, $\Delta u=1/(N\Delta x)$, and the summations over α and β account for aliasing. The sinc functions in Eq. (4) account for the finite extent of the measurements along the x and y dimensions. As long as the measured PSFs fit well within the area of the detector array, it is reasonable to approximate these sinc

functions as Dirac delta functions such that Eq. (4) can be written as

$$G_{p,q,k} \approx Z_{p,q,k} + \frac{1}{N\Delta x^2} \times \sum_{\alpha=-\infty}^{\infty} \sum_{\beta=-\infty}^{\infty} S[(p-\alpha N)\Delta u,(q-\beta N)\Delta u,d_k] \times \exp\left\{\frac{-i2\pi\Delta u}{N}[\hat{x}_k(p-\alpha N)+\hat{y}_k(q-\beta N)]\right\} \times H_d[(p-\alpha N)\Delta u,(q-\beta N)\Delta u]. \quad (5)$$

The Nyquist criterion [8,9] for adequately sampling $s(x,y,d_k)$ is $\Delta x < 1/B$, where B is the bandwidth of $s(x,y,d)$ along one dimension, i.e., $B=2f_0$, where $f_0 = D/(\lambda f)$ is the diffraction-limited cutoff spatial frequency for intensity detection. When the Nyquist criterion is satisfied, only the $\alpha=\beta=0$ summation terms contribute to $G_{p,q,k}$, for p and $q \in \{-N/2,(2-N)/2,\ldots,(N-2)/2\}$, and Eq. (5) reduces to an unaliased version of the continuous Fourier transform, i.e.,

$$G_{p,q,k} \approx Z_{p,q,k} + \frac{1}{N\Delta x^2} S(p\Delta u,q\Delta u,d_k) \times \exp\left[\frac{-i2\pi\Delta u}{N}(\hat{x}_k p+\hat{y}_k q)\right] H_d(p\Delta u,q\Delta u). \quad (6)$$

When the Nyquist condition is not satisfied, $G_{p,q,k}$ is corrupted by aliasing artifacts. Many imaging systems operate in this regime for reasons explained in [10]. Thus, when using complex pupil retrieval to characterize as-built imaging systems, one is likely to encounter aliasing.

This paper considers the effect that aliasing has on the ability to reconstruct $P(\xi,\eta)$. Section 2 describes a pupil retrieval algorithm that accounts for undersampling. Section 3 presents numerical simulation results that illustrate how algorithm performance degrades with undersampling when using a fixed number of PSF measurements in a baseline scenario. Section 4 describes two approaches for improving algorithm performance with undersampled data by making additional PSF measurements with (i) random misregistrations (x_k,y_k) or (ii) intermediate defocus amounts z_k. By intermediate defocus amounts, we mean system defocus settings between those used in the baseline scenario. While other multiplexing schemes are possible, we considered these two because they do not require additional hardware, as the misregistrations and intermediate defocus amounts can be realized by changes in the system pointing or focus, respectively. Section 5 is a summary. The algorithm presented here differs from that of [1] by accounting for the effects of finite-size pixels and undersampling in the Fourier domain instead of the spatial domain. Furthermore, the performance limits of both phase and pupil retrieval are explored for different amounts of undersampling.

2. PUPIL RETRIEVAL ALGORITHM

A. Data Consistency Metric

Given a particular estimate of the complex pupil function $\hat{P}(\xi,\eta)$, the corresponding PSFs $\hat{s}(x,y,d_k)$ can be computed through Eq. (1), replacing $P(\xi,\eta)$ with $\hat{P}(\xi,\eta)$, using fast Fourier transforms (FFTs) to compute DFT quantities as

$$s(m_f\Delta x_f,n_f\Delta x_f,d_k) = \left| \frac{1}{N} \sum_{p_f=-N/2}^{(N-2)/2} \sum_{q_f=-N/2}^{(N-2)/2} \hat{P}(\lambda f p_f\Delta u,\lambda f q_f\Delta u) \times \exp\left[\frac{-i2\pi}{N_f}(p_f m_f+q_f n_f)\right] \times \exp\left[\frac{-i8\pi d_k\Delta u^2}{D^2}(p_f^2+q_f^2)\right] \right|^2, \quad (7)$$

where $N_f \geq N$ and $\Delta x_f \leq \Delta x$ is a finer PSF sample spacing that satisfies the Nyquist sampling criterion and $N\Delta x = N_f\Delta x_f$. With estimated misregistrations $(\hat{x}_k,\hat{y}_k)$, the resulting PSF estimate $\hat{g}_{m,n,k}$ is given by the inverse DFT

$$\hat{g}_{m,n,k} = \frac{1}{N} \sum_{p=-N/2}^{(N-2)/2} \sum_{q=-N/2}^{(N-2)/2} \hat{G}_{p,q,k} \exp\left[\frac{i2\pi}{N}(mp+nq)\right], \quad (8)$$

where, allowing for aliasing,

$$\hat{G}_{p,q,k} = \sum_{\alpha=-\infty}^{\infty} \sum_{\beta=-\infty}^{\infty} \hat{S}[(p-\alpha N)\Delta u,(q-\beta N)\Delta u,d_k] \times \exp\left\{\frac{-i2\pi\Delta u}{N}[\hat{x}_k(p-\alpha N)+\hat{y}_k(q-\beta N)]\right\} \times H_d[(p-\alpha N)\Delta u,(q-\beta N)\Delta u], \quad (9)$$

and $\hat{S}(p_f\Delta u,q_f\Delta u,d_k)$ is computed as the 2D FFT of $\hat{s}(m_f\Delta x,n_f\Delta x,d_k)$. To avoid aliasing artifacts, these computations require $\hat{s}(x,y,d_k)$ to be sampled at or above the Nyquist rate, $\Delta x_f < 1/B$ (which will be finer than the actual detector-pixel pitch Δx for undersampled measurements), with N_f samples along the $x$and y directions. To obtain $\hat{S}(u,v,d_k)$ samples at the appropriate spacing for use in Eq. (9), the quantities Δx_f and N_f need to satisfy $N_f\Delta x_f = N\Delta x$. In practice, the α and β summations can be computed with finite limits, since $\hat{S}(u,v,d_k)$ is nonzero only over a region of width B in the Fourier domain.

The complex pupil retrieval algorithm used here employs a nonlinear optimization algorithm to iteratively search for a complex pupil function estimate $\hat{P}(\xi,\eta)$ that results in a $\hat{g}_{m,n,k}$ that best matches the measured data $g_{m,n,k}$. The algorithm also jointly estimates the misregistrations $(\hat{x}_k,\hat{y}_k)$. Here, the normalized mean squared error (NMSE) Φ between $\hat{g}_{m,n,k}$ and $g_{m,n,k}$ is used as a data consistency metric [11]:

$$\Phi = 1 - \frac{1}{K}\sum_{k=1}^{K} \frac{\left[\sum_{m=-N/2}^{(N-2)/2}\sum_{n=-N/2}^{(N-2)/2} w_{m,n,k}\, g_{m,n,k}\, \hat{g}_{m,n,k}\right]^2}{\left[\sum_{m=-N/2}^{(N-2)/2}\sum_{n=-N/2}^{(N-2)/2} w_{m,n,k}\, g_{m,n,k}^2\right]\left[\sum_{m=-N/2}^{(N-2)/2}\sum_{n=-N/2}^{(N-2)/2} w_{m,n,k}\, \hat{g}_{m,n,k}^2\right]}, \tag{10}$$

where $w_{n,m,k}$ is a window function that can be used to ignore bad pixels. This equation accounts for arbitrary scaling constants between $\hat{g}_{m,n,k}$ and $g_{m,n,k}$ for each k. The NMSE can be interpreted as the squared relative RMS error between $\hat{g}_{m,n,k}$ and $g_{m,n,k}$, i.e., $\Phi = 0.01$ is equivalent to a 10% RMS error between $\hat{g}_{m,n,k}$ and $g_{m,n,k}$. A conjugate-gradient routine was used for the optimization algorithm to obtain the pupil retrieval results shown later.

B. Gradient Expressions

The conjugate-gradient routine requires the gradient of the objective function with respect to the solution space variables, i.e., the gradient components $\partial\Phi/\partial\,\mathrm{Re}[\hat{P}(\xi,\eta)]$, $\partial\Phi/\partial\,\mathrm{Im}[\hat{P}(\xi,\eta)]$, $\partial\Phi/\partial\hat{x}_k$, and $\partial\Phi/\partial\hat{y}_k$. Alternatively, we could optimize over the amplitude and phase values of $\hat{P}(\xi,\eta)$ [1,2,5,12]. Efficient analytic computation of the gradient makes this approach computationally feasible. The derivation of the gradient equations is straightforward but lengthy. Since other papers contain these details for similar algorithms [1,4,5,12], only the steps related to the undersampling are shown here. Taking the partial derivative of Eq. (10) with respect to the sample values $\hat{g}_{m,n,k}$ yields

$$\frac{\partial\Phi}{\partial\hat{g}_{m,n,k}} = \frac{2}{K}\frac{\sum_{(m',n')} w_{m',n',k}\, g_{m',n',k}\, \hat{g}_{m',n',k}}{\left[\sum_{(m',n')} w_{m',n',k}\, g_{m',n',k}^2\right]\left[\sum_{(m',n')} w_{m',n',k}\, \hat{g}_{m',n',k}^2\right]} w_{m,n,k}\left[\hat{g}_{m,n,k}\frac{\sum_{(m',n')} w_{m',n',k}\, g_{m',n',k}\, \hat{g}_{m',n',k}}{\sum_{(m',n')} w_{m',n',k}\, \hat{g}_{m',n',k}^2} - g_{m,n,k}\right], \tag{11}$$

where compressed notation has been used for the double summations over all the samples m' and n'. Using the chain rule and Eq. (6), the partial derivatives with respect to the real and imaginary parts of the Fourier-domain samples $\hat{G}_{u,v,k}$ can be written as

$$\hat{G}_{p,q,k}^{\dagger} = \frac{\partial\Phi}{\partial\mathrm{Re}(\hat{G}_{p,q,k})} + i\frac{\partial\Phi}{\partial\mathrm{Im}(\hat{G}_{p,q,k})} = \frac{1}{N}\sum_{m=-N/2}^{(N-2)/2}\sum_{n=-N/2}^{(N-2)/2}\frac{\partial\Phi}{\partial\hat{g}_{m,n,k}}\exp\left[\frac{-i2\pi}{N}(mp+nq)\right]. \tag{12}$$

Note that this expression is valid for $|p|$ and $|q| \geqslant N/2$ by the periodicity of the DFT. Using the chain rule again with Eq. (9) gives the desired partial derivative with respect to $\hat{x}_k$:

$$\begin{aligned}\frac{\partial\Phi}{\partial\hat{x}_k} &= \sum_{(p_f,q_f)}\left[\frac{\partial\Phi}{\partial\mathrm{Re}(\hat{G}_{p_f,q_f,k})}\frac{\partial\mathrm{Re}(\hat{G}_{p_f,q_f,k})}{\partial\hat{x}_k} + \frac{\partial\Phi}{\partial\mathrm{Im}(\hat{G}_{p_f,q_f,k})}\frac{\partial\mathrm{Im}(\hat{G}_{p_f,q_f,k})}{\partial\hat{x}_k}\right] \\ &= \frac{-2\pi\Delta u}{N}\sum_{(p_f,q_f,\alpha,\beta)}(p_f-\alpha N)\mathrm{Im}\left\{\hat{G}_{p_f,q_f,k}^{\dagger}\hat{S}^*[(p_f-\alpha N)\Delta u,(q_f-\beta N)\Delta u,d_k]\right. \\ &\quad \left.\times\exp\left\{\frac{i2\pi\Delta u}{N}[\hat{x}_k(p_f-\alpha N)+\hat{y}_k(q_f-\beta N)]\right\}H_d^*[(p_f-\alpha N)\Delta u,(q_f-\beta N)\Delta u]\right\}.\end{aligned} \tag{13}$$

Likewise, the partial derivative with respect to $\hat{y}_k$ is

$$\begin{aligned}\frac{\partial\Phi}{\partial\hat{y}_k} = \frac{-2\pi\Delta u}{N}\sum_{(p_f,q_f,\alpha,\beta)}(q_f-\beta N)\mathrm{Im}\left(\hat{G}_{p_f,q_f,k}^{\dagger}\hat{S}^*[(p_f-\alpha N)\Delta u,(q_f-\beta N)\Delta u,d_k]\exp\left\{\frac{i2\pi\Delta u}{N}[\hat{x}_k(p_f-\alpha N)+\hat{y}_k(q_f-\beta N)]\right\}\right. \\ \left.\times H_d^*[(p_f-\alpha N)\Delta u,(q_f-\beta N)\Delta u]\right).\end{aligned} \tag{14}$$

Applying the chain rule again and using Eq. (9) yields

$$\hat{S}^{\dagger}(p_f\Delta u, q_f\Delta u, d_k) = \frac{\partial\Phi}{\partial \mathrm{Re}[\hat{S}(p_f\Delta u, q_f\Delta u, d_k)]} + i\frac{\partial\Phi}{\partial \mathrm{Im}[\hat{S}(p_f\Delta u, q_f\Delta u, d_k)]} = \hat{G}^{\dagger}_{p_f,q_f,k}\exp\left\{\frac{i2\pi\Delta u}{N}[\hat{x}_k(p-\alpha N)+\hat{y}_k(q-\beta N)]\right\}\times H_d^*[(p-\alpha N)\Delta u,(q-\beta N)\Delta u]. \quad (15)$$

Expressions for $\partial\Phi/\partial\,\mathrm{Re}[\hat{P}(\xi,\eta)]$ and $\partial\Phi/\partial\,\mathrm{Im}[\hat{P}(\xi,\eta)]$ can be obtained by repeated use of the chain rule with the specific equations used to compute $\hat{S}(f_x,f_y,z_k)$ from $\hat{P}(\xi,\eta)$. The details of doing this are contained elsewhere [1,4,5,12].

3. NUMERICAL SIMULATIONS

A. System Model

Numerical simulations were used to examine the performance of the pupil retrieval algorithm as the PSF sampling changes. A model of the James Webb Space Telescope (JWST) [13] was used as the optical system for the simulations. Table 1 lists the basic system parameters. The primary mirror is made up of 18 hexagonal segments. The gaps between segments can be seen in the amplitude of the pupil function for the telescope, shown in Fig. 1(a). The secondary mirror support struts are also visible in Fig. 1(a). The phase of the telescope pupil function is proportional to the wavefront aberration function. The wavefront aberration function used for the simulations is shown in Fig. 1(b). These aberrations are composed of random segment figure errors and segment piston, tip, and tilt misalignments.

In practice, the focal plane of the main telescope assembly is reimaged through various instruments in the science package. Suppose the telescope or one such instrument has a pupil mask (conjugate to the primary mirror of the telescope) to help suppress stray light. Figure 2(a) shows an example of such a mask that has the same overall shape as the primary mirror but is slightly larger to allow for small misalignments. The net system pupil function is then the product of the (demagnified) pupil of the primary mirror and the pupil mask. For the simulations, suppose there is a substantial misalignment of the pupil mask, as indicated by Fig. 2(b). Figure 2(c) shows the resulting amplitude of the pupil function $P(\xi,\eta)$ for the overall system. Figure 2(d) shows the wavefront error for the overall system. The peak-to-valley wavefront error is 0.78λ, and the RMS wavefront error is 0.12λ. In the absence of other diagnostic instruments, a complex pupil retrieval algorithm can be used to reconstruct $P(\xi,\eta)$ from PSF measurements to provide knowledge of the misalignment of the pupil mask and the combined aberrations of the system.

Table 1. Numerical Simulation Parameters

Parameter	Value
Encircled diameter of primary mirror, D	6.69 m
Focal length, f	131.4 m
F-number	19.6
Wavelength, λ	2.12 μm
PSF sample spacing, Δx_f	19.8 μm
Detector pixel pitch, Δx	19.8 to 104.1 μm
Detector sampling ratio, Q	0.4 to 2.1
Detector read noise (standard deviation)	5 photons
Average number of photons per PSF measurement	10^7 photons
Peak-to-valley defocus for PSF measurements	−1λ to +1λ
PSF misregistrations, (x_k,y_k) (standard deviation)	$5\Delta x$

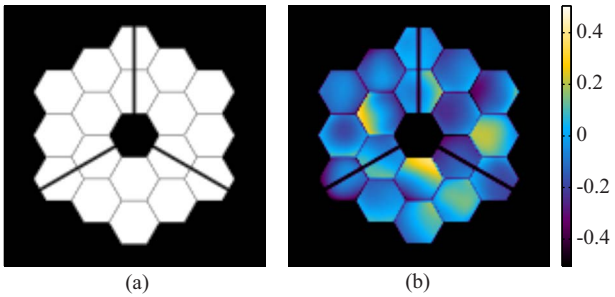

Fig. 1. (Color online) (a) Pupil function amplitude and (b) wavefront aberration function (in units of wavelengths) for the segmented-aperture telescope in the simulations.

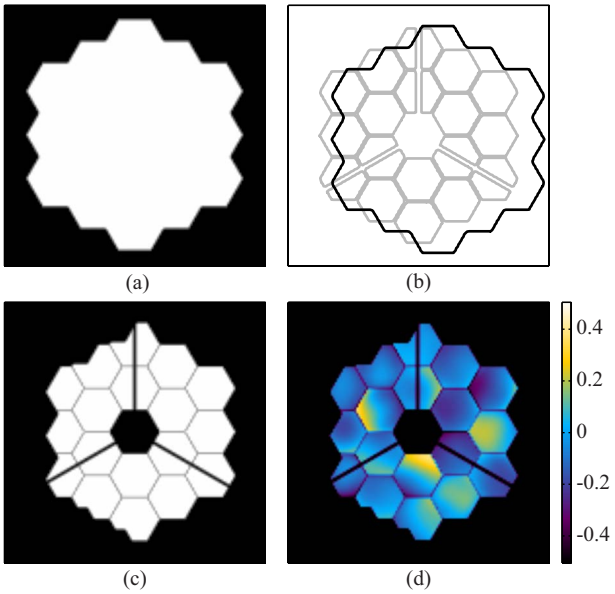

Fig. 2. (Color online) (a) Pupil mask used in conjunction with the segmented aperture of Fig. 1, (b) overlay of (gray curve) the segmented aperture and (black curve) the misaligned pupil mask, and the net system (c) pupil function amplitude and (b) wavefront aberration function.

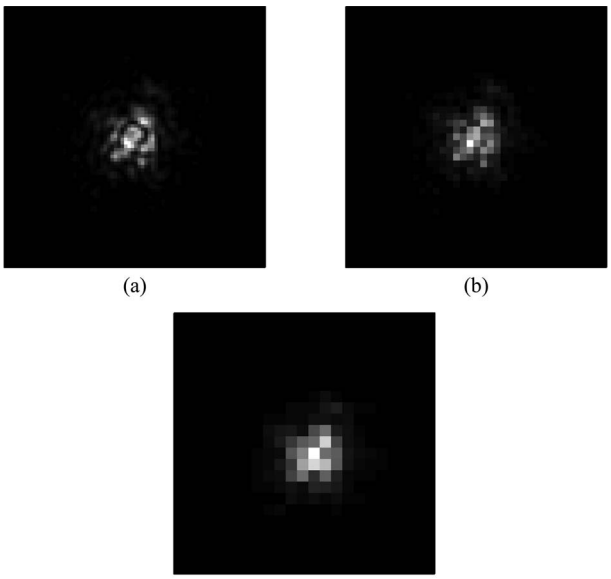

Fig. 3. Simulated PSF measurements for $d_k=-1\lambda$ of defocus and (a) $\Delta x=20.8$ μm, (b) $\Delta x=41.6$ μm, and (c) $\Delta x=69.4$ μm. The corresponding detector sampling ratios for (a), (b), and (c) are $Q=2.0$, 1.0, and 0.6.

PSF measurements were simulated by computing PSFs corresponding to the pupil function shown in Fig. 2 for defocus amounts $d_k=\{-1,0,1\}\lambda$ peak-to-valley of wavefront defocus across the full width of the primary mirror. Larger amounts of defocus are optimal for phase retrieval [14], but this smaller defocus was used to make the problem more challenging. The PSFs were then simulated according to Eqs. (7)–(9) and corrupted by noise to yield the PSF measurements $g_{m,n,k}$. The detector pixel impulse response was $h_d(x,y)=\text{rect}(x/\Delta x)\text{rect}(y/\Delta x)$, where $\text{rect}(x)=1$ for $|x|<1/2$ and $=0$ otherwise. The noise $\zeta_{m,n,k}$ was a combination of zero-mean Poisson-distributed shot noise and Gaussian-distributed read noise. The shot noise statistics were based on the average total number of photons per PSF measurement plane of 10^7 photons. Each PSF measurement was shifted by a random misregistration (x_k,y_k). Figure 3 shows simulated PSF measurements at various detector pixel pitch values. Notice that as Δx increases there are fewer samples across the bright portion of each PSF and the fine scale details of the PSF are lost.

B. Complex Pupil Retrieval Results

For each value of the detector pixel pitch Δx, a pupil function estimate $\hat{P}(\xi,\eta)$ was obtained from the simulated PSF measurements $g_{m,n,k}$ using the complex pupil retrieval algorithm described in Subsection 2.A. The algorithm also jointly estimated the PSF misregistrations $(\hat{x}_k,\hat{y}_k)$. The initial estimate used for the amplitude of $\hat{P}(\xi,\eta)$ is shown in Fig. 4, while the centroid of each PSF was used for the initial estimates of the $(\hat{x}_k,\hat{y}_k)$'s. A conjugate-gradient optimization routine was used to iteratively search for a $\hat{P}(\xi,\eta)$ that minimized the data consistency metric Φ. On each iteration, the conjugate-gradient algorithm would update $\hat{P}(\xi,\eta)$ based on the gradient components $\partial\Phi/\partial\text{Re}[\hat{P}(\xi,\eta)]$ and $\partial\Phi/\partial\text{Im}[\hat{P}(\xi,\eta)]$. Additionally, knowledge of the pupil function extent was incorporated into the algorithm by multiplying these gradient components by a window function $W(\xi,\eta)$ that is equal to unity for $\rho\leq 0.5D$, zero for $\rho\geq 0.525D$, and

Fig. 4. Initial pupil function estimate used for the retrieval algorithm.

$$W(\xi,\eta)=\cos^2[0.5\pi(\rho-0.5D)/(0.025D)], \tag{16}$$

for $0.5D<\rho<0.525D$, where $\rho=\sqrt{\xi^2+\eta^2}$. This $W(\xi,\eta)$ is equal to the initial estimate for $\hat{P}(\xi,\eta)$ shown in Fig. 4. This approach does not allow the algorithm to update $\hat{P}(\xi,\eta)$ for pupil samples where $W(\xi,\eta)=0$, which ensures that the pupil estimate will have approximately the correct width. Results were obtained by running the algorithm for 2,000 and 10,000 iterations.

Two metrics were used to quantify the performance of the complex pupil retrieval algorithm: (i) the normalized (RMS) error E of $\hat{P}(\xi,\eta)$, and (ii) (RMS) error σ of $\arg[\hat{P}(\xi,\eta)]$ for samples within the support of the true pupil function. The first metric is computed as

$$E^2=\min_{(c,\varphi_0,t_\xi,t_\eta,\xi_0,\eta_0)}\left\{\frac{\sum_{(\xi,\eta)}|c\exp[i\varphi_0+it_\xi(\xi-\xi_0)+it_\eta(\eta-\eta_0)]\hat{P}(\xi-\xi_0,\eta-\eta_0)-P(\xi,\eta)|^2}{\sum_{(\xi,\eta)}|P(\xi,\eta)|^2}\right\}, \tag{17}$$

where c, φ_0, t_ξ, t_η, ξ_0, and η_0 are parameters that account for an arbitrary multiplicative scaling factor; piston, tip, and tilt phase terms; and horizontal and vertical translations, respectively, in $\hat{P}(\xi,\eta)$ [11]. E is interpreted as the relative error for the retrieved pupil function; i.e., $E=0.15$ corresponds to a relative error of 15% in $\hat{P}(\xi,\eta)$. The summations in Eq. (17) are over all of the (ξ,η) pupil plane samples. The second metric is computed as

$$\sigma^2 = \frac{1}{N_{\chi(\xi,\eta)\in\chi}} \sum \arg^2\left\{ \frac{\exp[i\varphi_0 + it_\xi\xi + it_\eta\eta]\hat{P}(\xi-\xi_0,\eta-\eta_0)}{P(\xi,\eta)} \right\}, \tag{18}$$

where the summation includes pupil plane samples only within the set $\chi=\{(\xi,\eta):|P(\xi,\eta)|>0.05\}$ and N_χ is the number of samples in χ. For reference, a $\hat{P}(\xi,\eta)$ with a completely random phase error uniformly distributed over $[-\pi,\pi]$ would yield $\sigma=\pi/\sqrt{3}=0.29\lambda$.

Figure 5 shows how F and σ varied with the detector pixel pitch Δx or the sampling ratio $Q=\lambda f/D\Delta x$. Phase retrieval results obtained using knowledge of the true pupil amplitude are also shown for comparison. These plots clearly indicate the degradation of the estimated pupil quantities associated with undersampling. For complex pupil retrieval, the quality of the estimated phase was better than $\lambda/20$ RMS down to about $Q=1$. Figure 6 shows images of the retrieved pupil amplitude and phase (across the true aperture) at different values of Q. For $Q=2$, the results were excellent. For $Q=1$, the retrieved amplitude had the correct coarse features but appears rather noisy; nevertheless, the retrieved phase was quite good. The results were poor for $Q=0.6$. For phase retrieval (assuming the pupil amplitude is known), on the other hand, the retrieved phase was better than $\lambda/20$ RMS for values of Q down to almost 0.6.

Among the factors that contribute to the drop in performance with increasing Δx (decreasing Q), two interdependent effects of are particular interest. First, there are fewer measurement samples across the bright portion of the PSF as Δx increases, as illustrated in Fig. 3. This makes the inverse problem more difficult, as there are fewer samples from which to retrieve the same number of pupil samples. Second, aliasing artifacts lead to ambiguities in the data. Once the fine spatial details of the PSF are aliased to lower spatial frequencies, it is not always possible to sort out the coarse and fine details of the true PSF from the data. Because the amount of aliasing increases as the number of samples decreases, these effects are not separable for the scenario considered here. Section 4 demonstrates two strategies that address these issues to improve complex pupil retrieval performance at smaller values of Q.

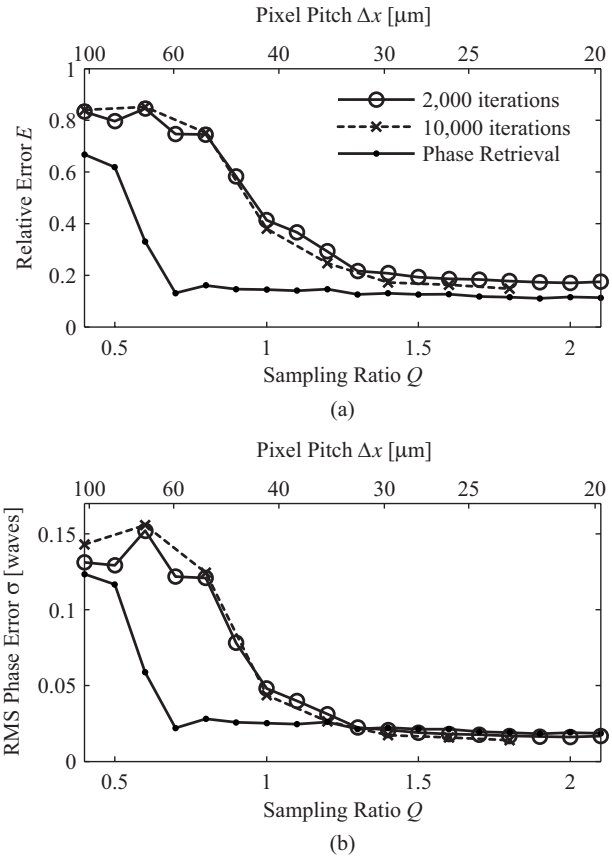

Fig. 5. Complex pupil retrieval results for the baseline scenario using three PSF measurements versus the detector sampling ratio after (open circles) 2,000 iterations and (x's) 10,000 iterations. Phase retrieval results are also shown for comparison.

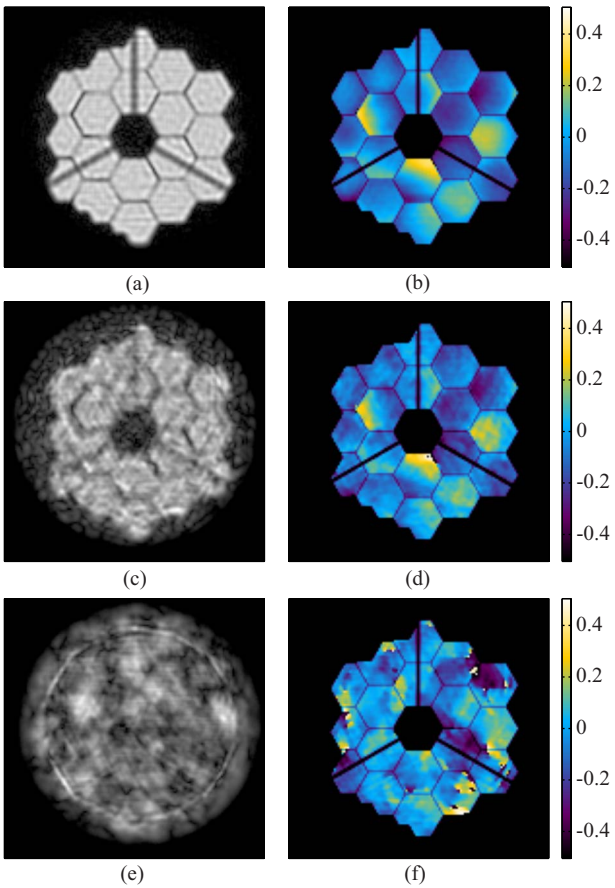

Fig. 6. (Color online) Retrieved (left column) pupil amplitude and (right column) wavefront aberration functions for (top row) $Q=2.0$, (middle row) $Q=1.0$, and (bottom row) $Q=0.6$ for the baseline scenario using three PSF measurements.

4. IMPROVED PERFORMANCE

A. Random Misregistrations

The generalized sampling theorem [15] states that a band-limited signal can be reconstructed from a set of aliased measurements (i.e., that do not satisfy the Nyquist sampling criterion), provided that (i) there are enough measurement sets and (ii) the sample locations for the various measurement sets are nonredundant. This theorem is the basis of multiframe detector superresolution algorithms that process a number of aliased images of the same scene to yield a single dealiased image with enhanced spatial resolution [16]. The same principle can be used to overcome problems with aliasing for pupil retrieval by recording multiple PSF measurements with random misregistrations (x_k, y_k) at each defocus setting. Figure 7 shows the complex pupil retrieval results obtained using four PSF measurements at each defocus setting as before for a total of $K=12$ PSF measurements (all of the other simulation parameters were the same as for the results shown in Fig. 5). This corresponds to using random pointing fluctuations of the system to acquire additional PSF measurements with nonredundant sampling. As expected, the quality of the estimated pupil quantities was improved at smaller values of Q in comparison with Fig. 5. Using the extra PSF measurements enabled the pupil phase to be estimated with $\lambda/20$ RMS error down to $Q=0.7$. Figure 8 shows example images of the retrieved pupil amplitude and phase for $Q=2$, 1, and 0.6. In this case, the results for $Q=1$ appear almost as good as the results obtained for $Q=2$ using only three PSF measurements (see Fig. 6). Ideally, one would expect these results to be equivalent based on the generalized sampling theorem, but there is an additional signal-to-noise ratio penalty associated with the detector transfer function $H_d(u,v)$ at higher spatial frequencies for aliased data. The results for $Q=0.6$ shown in Fig. 8 are about equivalent to the results obtained for $Q=1$ using fewer PSFs shown in Fig. 6. The results of phase retrieval benefited as well, although not by as much.

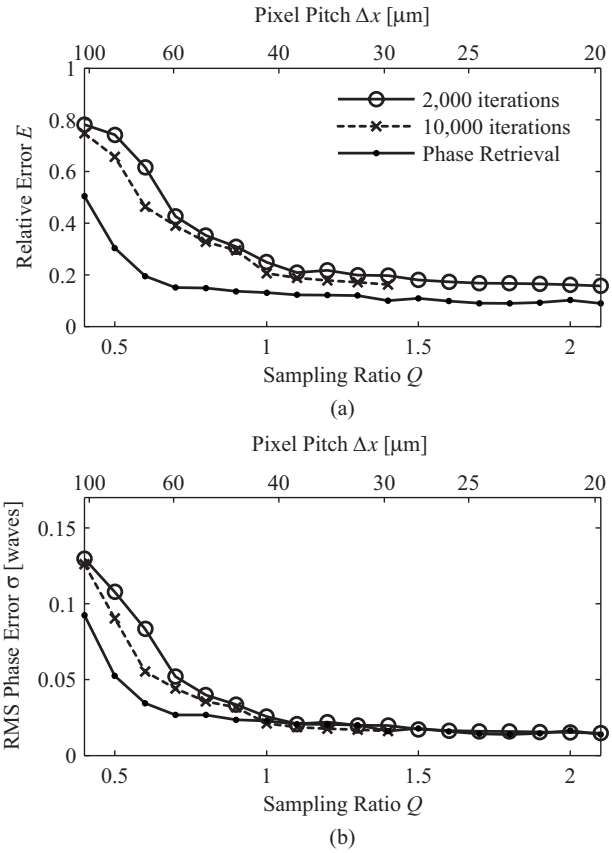

Fig. 7. Same as Fig. 5 except for the scenario using 12 PSF measurements (4 measurements with random pointing fluctuations at each of 3 defocus settings).

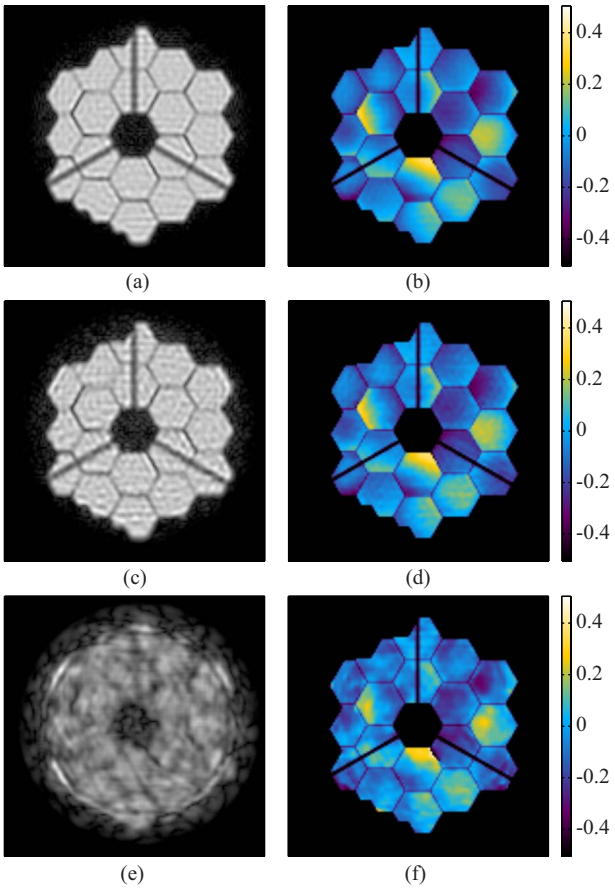

Fig. 8. (Color online) Retrieved (right column) pupil amplitude and (left column) wavefront aberration functions for (top row) $Q=2.0$, (middle row) $Q=1.0$, and (bottom row) $Q=0.6$ using 12 PSF measurements (4 measurements with random pointing fluctuations at each of 3 defocus settings).

B. Intermediate Defocus Values

Another strategy for improving the performance of the pupil retrieval algorithm is to make additional PSF measurements at intermediate defocus settings with no misregistrations. While the generalized sampling theorem is not directly applicable to this scenario, the additional measurements contain nonredundant information (due to intermediate defocus amounts) that should mitigate aliasing effects. Figure 9 shows the complex pupil retrieval results obtained from a set of $K=12$ PSF measurements with defocus values of $\{\pm 1/6, \pm 1/3, \pm 1/2, \pm 2/3, \pm 5/6, \pm 1\}$ λ peak-to-valley across the full width of the primary. The algorithm used knowledge that the misregistrations were zero, and the misregistration parameters were not optimized. These results are

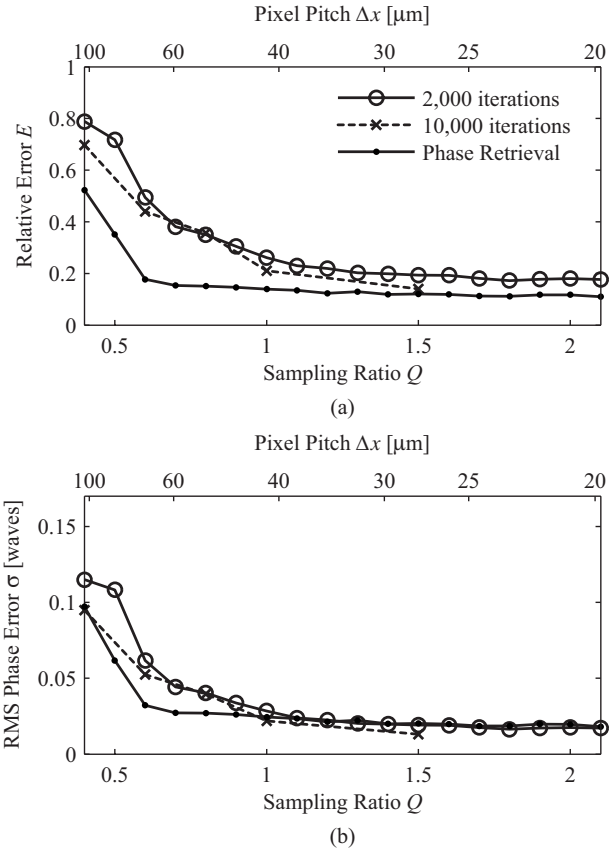

Fig. 9. Same as Fig. 5 except for scenario using 12 PSF measurements at intermediate defocus values with no misregistrations.

comparable to the random misregistration case and are better than the case of using three PSF measurements at only three defocus settings.

The fact that the defocus results are practically equivalent to the misregistration case suggests that the generalized sampling theorem is more widely applicable to measurement scenarios involving nonlinear transformations. By this we mean that it appears to be possible to reconstruct a bandlimited signal from aliased measurements, provided that there are a sufficient number of nonredundant measurements, *even if the measurements involve nonlinear operations*. A proof of this is beyond the scope of this paper.

5. SUMMARY

Complex pupil retrieval can be used to estimate the complex-valued pupil function (amplitude and phase) of an imaging system from PSF measurements made in various defocus planes. For a fixed number of PSF measurements, the quality of the retrieved pupil amplitude and phase deteriorates as the detector pixel pitch increases and the detector sampling ratio Q decreases. Two contributing factors were noted in this regard. First, there are fewer measurement samples across the bright portion of the PSF for larger pixels and, thus, less data to use for retrieving the pupil function. Second, aliasing artifacts can introduce ambiguities in the data. Two strategies were demonstrated for improving the pupil retrieval results by collecting additional PSF data with either (i) misregistrations produced by random pointing fluctuations or (ii) intermediate amounts of defocus (or both). Each of these methods substantially improved the reconstructions. Another approach, not considered here, is to incorporate additional knowledge about the pupil function into the pupil retrieval algorithm [5].

ACKNOWLEDGMENT

This work was funded by NASA Goddard Space Flight Center.

REFERENCES

1. J. R. Fienup, "Phase retrieval for undersampled broadband images," J. Opt. Soc. Am. A **16**, 1831–1837 (1999).
2. S. M. Jefferies, M. Lloyd-Hart, E. K. Hege, and J. Georges, "Sensing wave-front amplitude and phase with phase diversity," Appl. Opt. **41**, 2095–2102 (2002).
3. P. Almoro, G. Pedrini, and W. Osten, "Complete wavefront reconstruction using sequential intensity measurements of a volume speckle field," Appl. Opt. **45**, 8596–8605 (2006).
4. G. R. Brady and J. R. Fienup, "Nonlinear optimization algorithm for retrieving the full complex pupil function," Opt. Express **14**, 474–486 (2006).
5. S. T. Thurman, R. T. DeRosa, and J. R. Fienup, "Amplitude metrics for field retrieval with hard-edge and uniformly illuminated apertures," J. Opt. Soc. Am. A **26**, 700–709 (2009).
6. J. W. Goodman, *Introduction to Fourier Optics*, 3rd ed. (Roberts, 2005).
7. S. T. Thurman and J. R. Fienup, "Wiener reconstruction of undersampled imagery," J. Opt. Soc. Am. A **26**, 283–288 (2009).
8. E. T. Whittaker, "On the functions which are represented by the expansions of the interpolation theory," Proc. - R. Soc. Edinburgh, Sect. A: Math. **35**, 181–194 (1915).
9. H. Nyquist, "Certain topics in telegraph transmission theory," Trans. Am. Inst. Electr. Eng. **47**, 617–644 (1928).
10. R. D. Fiete, "Image quality and λ FN/p for remote sensing systems," Opt. Eng. **38**, 1229–1240 (1999).
11. J. R. Fienup, "Invariant error metrics for image reconstruction," Appl. Opt. **36**, 8352–8357 (1997).
12. J. R. Fienup, "Phase retrieval algorithms for a complicated optical system," Appl. Opt. **32**, 1737–1746 (1993).
13. http://www.jwst.nasa.gov/
14. J. J. Green, B. H. Dean, C. M. Ohara, D. C. Redding, and Y. Zhang, "Target selection and imaging requirements for JWST fine phasing," Proc. SPIE **5487**, 944–953 (2004).
15. A. Papoulis, "Generalized sampling expansion," IEEE Trans. Circuits Syst. **CAS-24**, 652–654 (1977).
16. S. C. Park, M. K. Park, and M. G. Kang, "Super-resolution image reconstruction: a technical overview," IEEE Signal Process. Mag. **20**, 21–36 (2003).